Mechanisms of Long-Range Energy Transfer from Quantum Dots to Black Phosphorus

Suyog Padgaonkar^{a†}, Paul T. Brown^{b†}, Yeonjun Jeong^a, Charles Cherqui^a, Kobra N. Avanaki^{a,c}, Rafael López-Arteaga^a, Shawn Irgen-Gioro^a, Yue Wu^a, Vinod K. Sangwan^b, Brendan Kerwin^a, George C. Schatz^a, Mark C. Hersam^{*a,b}, and Emily A. Weiss^{*a,b}

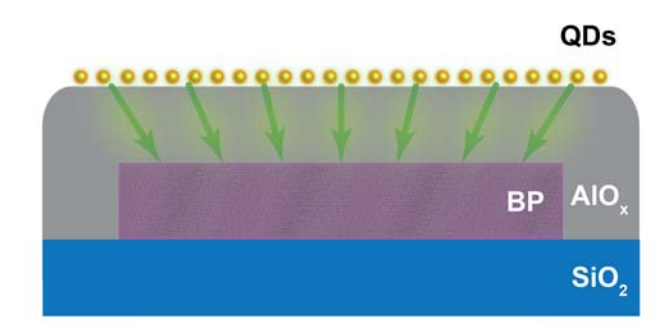
Departments of ^aChemistry and ^bMaterials Science and Engineering, Northwestern University, Evanston, IL 60208

^cDepartment of Chemistry and Chemical Biology, Harvard University, Cambridge, MA 02138 [†]These authors contributed equally.

Abstract: This study explores the mechanisms of long-range energy transfer (EnT) from a self-assembled film of CdSe/ZnS core-shell quantum dots (QDs) to black phosphorus (BP) nanoflakes through an AlO_x encapsulation layer of variable thickness. The dependence of the EnT rate on donor-acceptor distance, d, scales as $\sim d^{-2.3}$, which is shallower than the theoretical scaling of $\sim d^{-3}$ for Förster-type EnT from a zero-dimensional (0D) donor to a three-dimensional (3D) acceptor. Electrodynamic simulations reveal that the efficient long-range EnT is attributable to the high areal concentration of the QD film, which results in scattering of a donor QD's dipole field by neighboring QDs, thereby effectively increasing the area over which the donor and acceptor couple. The demonstration of efficient photosensitization of BP through a passivating dielectric layer is important for the development of high-performance optoelectronic devices based on ambient-reactive layered semiconductors.

^{*}corresponding authors. Emails: e-weiss@northwestern.edu, m-hersam@northwestern.edu

TOC Image:



Black phosphorous (BP) is a promising layered two-dimensional (2D) semiconductor for optoelectronic applications due to high carrier mobility (>10² cm/Vs at room temperature) and direct bandgap at all thicknesses ranging from near-infrared to mid-infrared wavelengths.^{1,2} However, BP shows dramatic chemical reactivity upon exposure to ambient conditions, such as air, light, and water,³ and therefore, facile and scalable encapsulation schemes, such as atomic layer deposition of alumina (AlO_x), are required for long-term stability necessary for practical applications.^{4,5} In general, these encapsulation layers are considered extraneous and do not participate in the operating mechanism of the devices. Given notable electron and hole mobilities, one promising application of BP enabled by its encapsulation is as a charge transport layer in photodetectors. While BP is not a strong absorber itself (absorption cross-sections of 10⁻¹⁶ cm² at 515 nm), which limits its responsivity in photodetector applications, 8,9 performance of these devices can be improved by photosensitizing BP by another light-absorbing material. In this scenario, energy must be subsequently transferred from the photosensitizer to the BP, through the encapsulation layer. 10,111 Such energy transfer (EnT) must be accomplished in high yield over several nanometers, since, for instance, a minimum of 3 nm of AlO_x is required for indefinite chemical stability of BP.4 For this purpose, Förster-type EnT is a viable sensitization strategy because it occurs through near-field electromagnetic coupling and has been observed to occur at yields of >50% even when donor-acceptor distances are 35 nm. 12,13 This long-range mechanism stands in contrast with charge transfer, which has proved effective in using semiconductor quantum dots (QDs) to photosensitize ambient-stable 2D materials such as graphene.¹⁴

In the point-dipole implementation of Förster theory, which is only appropriate for describing systems with zero-dimensional (0D) donors and acceptors, the rate and yield of EnT scales with the donor-acceptor distance, d, as $\sim d^{-6}$. Modifications to this simple model must be made in studies of systems with higher dimensionality, where, experimentally, scalings of $\sim d^{-4}$ in 0D donor-2D acceptor systems and $\sim d^{-2}$ in 2D-2D systems have been observed. Other studies have found that parameters such as the thickness of a 3D acceptor can perturb the distance dependence of EnT. Representation, the magnitude of the electromagnetic coupling that mediates EnT is sensitive to many structural and electronic parameters of the donor-acceptor system; so, to maximize the yield of photosensitization, we must characterize the distance-dependence of Förster-type EnT for each system of interest, and develop models to link that distance dependence to as many parameters as possible.

Here, we photosensitize multilayer BP with 0D semiconductor QDs, which have large absorbance cross-sections and high photoluminescence quantum yields. QDs are common choices for photosensitizing 2D materials, but these studies have been so far been limited to materials that are stable in ambient conditions and therefore unencapsulated. 13,17-28 Our mixed-dimensional system comprises a monolayer film of close-packed CdSe/ZnS QDs deposited on AlOxencapsulated BP nanoflakes. By varying the thickness of the AlO_x layer between 3 and 20 nm, we determine that the rate of EnT scales as $\sim d^{-2.3}$, and the Förster radius, where the probability of EnT from QD to the BP equals the probability of QD exciton decay, is 11 nm. Finite difference time domain (FDTD) simulations of the electrodynamic interactions within our system allow us to attribute this shallow distance dependence and large Förster radius to i) the 3D nature of the BP acceptor (at a thickness of 20-30 nm, the flakes are electronically bulk-like),⁶ and ii) the pseudo-2D nature of the close-packed monolayer of QDs, which enables electrodynamic interactions within the donor sheet, ²⁹ in contrast with prior studies that used isolated single particles or more dilute films of QD donors. 16-19,21,22,24,30 Thus, our study provides a general strategy for long-range photosensitization of ambient-reactive materials through their encapsulation layers that is translatable to a wide variety of photosensitizers and 2D charge transport layers.

Figure 1a shows a schematic diagram of our system. We synthesized CdSe/ZnS QDs with an average diameter of 4.7 ± 0.7 nm and peak emission wavelength of 530 nm using reported procedures, see the Supporting Information ("SI"). 31,32 We obtained isolated BP flakes through micromechanical exfoliation from commercial crystals onto 300-nm SiO₂/Si substrates, and encapsulated the BP flakes with atomic layer deposition (ALD) of AlO_x with thicknesses between 3 nm and 20 nm. 4,33 Unencapsulated BP degrades within minutes of exposure to air due to reactions with ambient oxygen and water, 34 but we observe no signs of degradation in air after four weeks of encapsulation, consistent with previous reports (see the SI). We deposited a close-packed monolayer film of the QDs self-assembled at the liquid-air interface onto the surfaces of the AlO_x-coated BP flakes using a method described in the SI and elsewhere. This method produces a densely covered substrate, as seen in the fluorescence lifetime imaging microscope (FLIM) image, **Figure 1b**, and equal coverage on and off the BP flakes, as measured by atomic force microscopy (AFM, see the SI).

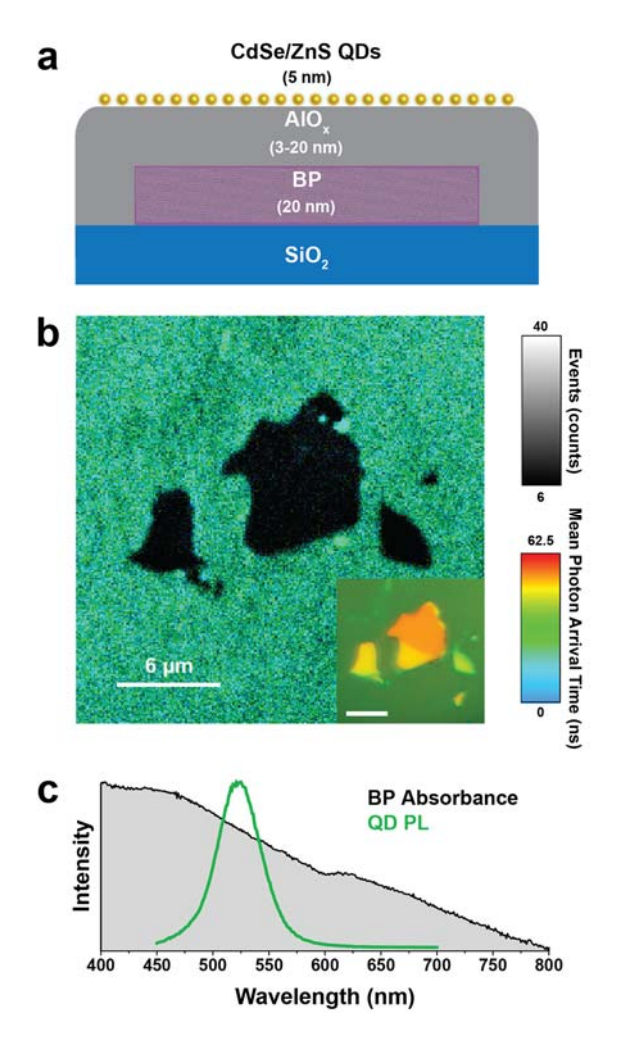


Figure 1. (a) Schematic of QD/AlO_x/BP system, not to scale. (b) FLIM map of a QD monolayer film deposited on 3 nm of ALDgrown AlO_x on exfoliated BP, on an Si/SiO₂ substrate. The top grayscale bar (black to white) indicates the intensity of the PL in the FLIM map. The bottom color bar (blue to red) indicates the average lifetime of the PL in the FLIM map. Inset: Optical image of the same area, with the same scale bar. (c) absorbance Ground-state spectrum exfoliated BP on glass (black) and emission spectrum of CdSe/ZnS QDs (green). The yaxis has arbitrary units as the graph is intended to show overlap of the two spectra. The discontinuity in the absorbance at ~ 625 nm is due to a grating change in the spectrometer.

The FLIM map, Figure 1b, also confirms that deposition of the QDs on the BP flake quenches their photoluminescence (PL). This result indicates that BP introduces a competitive nonradiative decay process for excitons in the QDs. Although we cannot monitor the PL of the acceptor (BP) because its emission is in the midinfrared spectral region and outside the range of our detector, we provide experimental evidence supporting Forster-type EnT such as (i) the spectral overlap of the emission of the QDs and the broad absorbance of BP, Figure 1c, and (ii) the ≥ 6 nm insulating barrier (comprised of a ~ 1 nm ZnS shell, ~2-nm oleate/octadecylamine ligand shell, and >3-nm AlO_x layer), which prohibits electron transfer from the conduction band of photoexcited CdSe QDs to the conduction band (CB) of BP, even though it is energetically allowed.³⁶ Dexter-type EnT, a semi-concerted transfer of both electron and hole, is eliminated for the same reason.

Time-resolved PL (TRPL) traces, **Figure 2a**, extracted from FLIM maps like that shown in **Figure 1b** show that the lifetime of the QD exciton increases monotonically as the distance between QD and BP increases, as controlled by the thickness of AlO_x encapsulation. **Figure 2b** is a plot of the amplitude-averaged lifetime of the QD exciton, calculated from multi-exponential fits of the traces in **Figure 2a**, as a function of the donor-acceptor (QD-BP)

distance, which includes the 2.5-nm radius of the QD (see TEM images in the SI), the estimated 2.4-nm length of the oleate/octadecylamine ligands on the QD surfaces, and the \geq 3-nm AlO_x encapsulation layer on BP. Without underlying BP, the amplitude-averaged PL lifetime, $\tau_{ex,0}$, of the QDs deposited on AlO_x is 10.4 ns. In presence of BP encapsulated by 3-nm AlO_x, the average PL lifetime of the QDs, τ_{ex} , decreases to 3.7 ns. With increasing thickness of AlO_x, the PL lifetime increases, eventually reaching 9.7 ns for a 20-nm-thick AlO_x layer (the thickest layer in this study), which is within 8% of the lifetime measured in the absence of BP, **Figures 2a,b**.

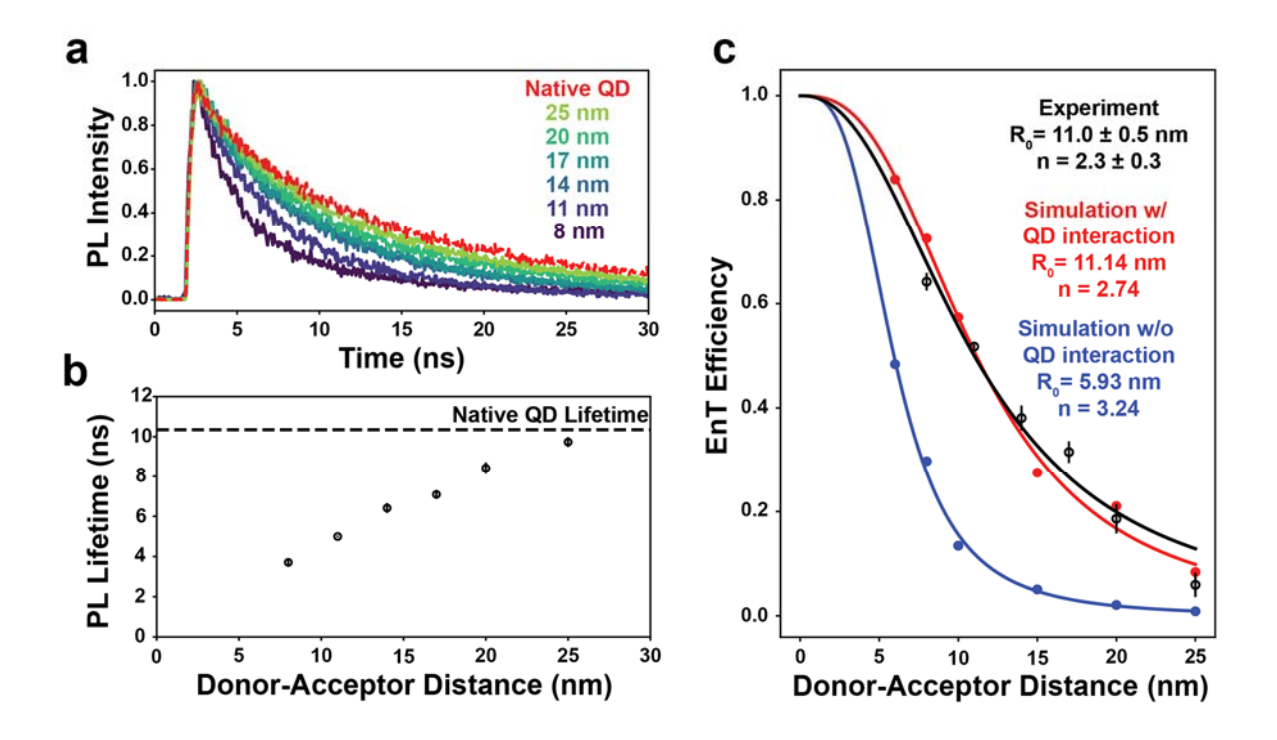


Figure 2. (a) Decay of the PL of the QDs deposited on BP with time after excitation, for AlO_x spacer layers of varying thickness; the legend shows the corresponding total donor-acceptor distances. "Native QD" corresponds to QDs deposited on AlO_x without underlying BP. These kinetic traces are averaged across three to five measurements at separate locations on the BP flakes for each AlO_x thickness; see the SI for error analysis. **(b)** Amplitude-averaged excitonic lifetime determined from bi-exponential fits of the traces in (a), see the SI, as a function of donor-acceptor distance. The dashed line is the native QD lifetime. **(c)** Experimental EnT efficiency, defined by eq 2 of the main text, as a function of donor-acceptor distance, fit with nonlinear regression (black). Simulations of this quantity with (red) and without (blue) QD interactions (scattering and absorption of the electric field from photoexcited QDs by the surrounding QDs).

We calculate the EnT rate as in eq 1, assuming

$$k_{EnT} = \frac{1}{\tau_{ex}} - \frac{1}{\tau_{ex,0}} \tag{1}$$

that EnT is the sole non-radiative process that accelerates exciton decay in the presence of BP, 37 and define the EnT efficiency, E, by eq 2. **Figure 2c** (black) is a plot of the EnT efficiency versus

$$E = 1 - \frac{\tau_{ex}}{\tau_{ex0}} \tag{2}$$

the donor-acceptor distance, fit with

$$E = \frac{R_0^n}{R_0^n + d^n} \tag{3}$$

where d is the variable donor-acceptor distance (from the center of the donor QD to the surface of the acceptor BP), R_o is the effective Förster radius, at which the probability of EnT is equal to the probability of native radiative or nonradiative processes within the QD, and n is related to the total dimensionality of the system.^{38,39} This fit yields $n = 2.3 \pm 0.3$ and $R_o = 11.0 \pm 0.5$ nm, which is 3 nm longer than the donor-acceptor distance (8 nm) corresponding to the minimum thickness of AlO_x required to stabilize BP (3 nm).

When the donor-acceptor distance is small compared to the wavelength of the photons being transmitted, quasistatic image dipole theory predicts that the rate of EnT from an isolated 0D donor to a 3D acceptor has a distance dependence of d^{-3} and that this trend should still hold even in the presence of an encapsulation layer (see more details in the SI).^{40,41} The longest donor-acceptor distance in this experiment is ~25 nm, so the quasistatic approximation is valid. To explain the value of n (2.3 ± 0.3) we obtain by fitting the experimental data in **Figure 2c** to eq 3, we propose that the distance dependence of EnT in our system is influenced by scattering of the dipole fields of photoexcited QD donors by nearby QDs, which changes the spatial profile of the emitted electric field. From the quantum mechanical point of view, this scattering amounts to EnT to other QDs before absorption by BP.

To model the system with many QDs and the acceptor, we used finite-difference time-domain (FDTD) simulations. We calculated the EnT efficiency from many photoexcited QDs to BP in two cases: (i) where the QDs interact with the electric field emitted by the other QDs, and (ii) where they do not. In these simulations, QDs that can scatter or absorb the electric field of other QDs are modeled as electric dipole sources enclosed by a dielectric sphere using a Lorentz model that includes the resonance response of the QD, and hypothetical non-interacting QDs are simply described as dipole sources without dielectric spheres (see the SI for more details).⁴² In both cases,

we placed 100 QD dipole sources of the same magnitude and phase, as well as random orientations and positions, within a 200 nm × 200 nm region on an alumina layer (refractive index 1.7682) of varying thickness. This concentration of QDs on the alumina layer is smaller than but comparable to the experiment. A 35 nm-thick BP layer was placed below the alumina layer. We applied a periodic boundary condition in the *x* and *y* directions to repeat this 200 nm × 200 nm unit cell. To describe the broadband absorption of BP, its relative perimittivity was modeled as a superposition of Lorentz models (see the SI). We note that we have not considered that the ALD-grown AlO_x used in the experiment is likely amorphous, which may result in mild absorption by the alumina layer and therefore affect the distance dependence and Förster radius. The absorption power of the BP layer was obtained and converted to the EnT rate using,

$$\frac{k_{EnT}}{k_0^{QD}} = \frac{P_{abs}^{BP}}{P_0^{QD}} \tag{4}$$

where k_{EnT} is the EnT rate, k_0^{QD} is the emission rate of a native QD (the inverse of the lifetime multiplied by the measured quantum yield, QY of 52%), P_{abs}^{BP} is the simulated BP absorption power in one unit cell, and P_0^{QD} is the emission or power of the QDs in one unit cell. To consider the finite emission lineshape of QDs, we calculated P_{abs}^{BP} as

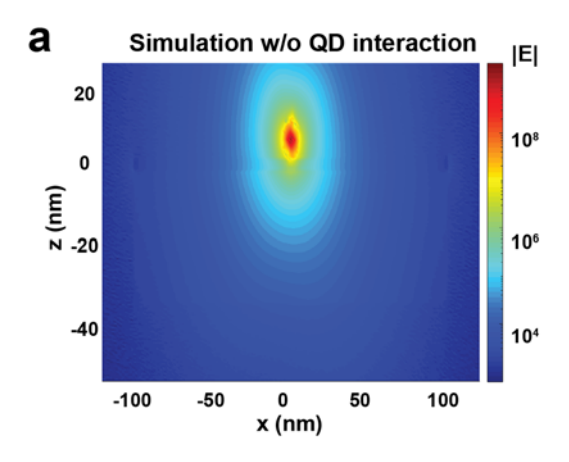
$$P_{abs}^{BP} = \frac{\sum_{i} P_{abs}(\omega_i) I_D^{emi}(\omega_i)}{\sum_{i} I_D^{emi}(\omega_i)},$$
 (5)

where $P_{abs}(\omega)$ is the frequency-dependent absorption power of the BP layer and $I_D(\omega)$ is the emission spectrum of a native QD (modeled as a Gaussian function with a mean at 550 nm and a standard deviation of 15 nm). The sum was performed over 101 linearly spaced frequency points spanning the wavelength range 500-600 nm. In case where the dipole sources were enclosed by dielectric spheres, we applied a frequency-dependent correction factor to $P_{abs}(\omega)$ that accounts for the change of the emitted power from the dipole–sphere composite structure due to the response of the dielectric sphere. Once we obtained k_{EnT} , the EnT efficiency, E, was calculated as follows (using τ^{QD} =10.5 ns).

$$E = \frac{k_{EnT}}{k_{EnT} + k_0^{QD} + k_{nr}^{QD}} = \frac{k_{EnT}}{k_{EnT} + 1/\tau^{QD}}$$
(6)

Figure 2c (red, blue) shows the calculated EnT efficiency E as a function of the donor-acceptor distance. When QDs in the simulation include dielectric spheres that allow interaction with the electric field emitted by the other QDs, the R_0 increases from 5.93 nm to 11.1 nm. This agrees well with the experimental value of 11.0 nm. The distance dependence of the EnT rate is

 $d^{-3.2}$ for non-interacting QDs (as expected from the quasistatic image dipole theory for an isolated



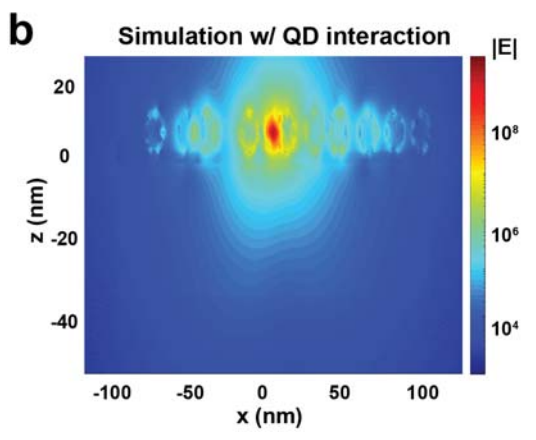


Figure 3. FDTD simulations of the spatial profile of the magnitude of the electric field |E| generated by a single excited QD modeled as a dipole source enclosed by a dielectric sphere (a) isolated and (b) surrounded by 10 ground-state QDs (dielectric spheres). The BP and the alumina layer spanned the region by $-100 \, nm < x < 100 \, nm$, defined -100 nm < y < 100 nm, and -35 nm <z < 0 nm (BP) and 0 nm < z < 3 nm(alumina). The centers of all QDs were on the xz plane at z = 8 nm. The center of the excited OD was at the origin, and the orientation of its dipole source was defined by spherical coordinates $\theta = 124^{\circ}$ and $\phi =$ 0° . The figures are the slices at y = 0 nm. The same dielectric functions for BP, alumina, and the QDs as those used for the calculation of the EnT efficiency were used.

QD described above) and $d^{-2.7}$ for interacting QDs, which is closer to the experimental scaling of $d^{-2.3\pm0.3}$.

The simulations suggest that we attribute the unexpectedly long Förster radius and shallow distance dependence of the EnT rate in the mixed dimensional BP-QD system to QD-QD electrodynamic interactions. When QDs interact with one another, an excited QD can transfer its excitonic energy in the lateral direction to the nearby QDs before the energy is absorbed by the BP, as illustrated by the FDTDcalculated electric field profiles in Figure 3.⁴³ This interaction widens the effective area of BP that interacts with the initially excited QD, opening non-vertical channels for EnT. The lengths of these channels increase sub-linearly with increasing d, thus reducing the overall distance dependence of the EnT rate. Further insights are provided by alternative derivations of the energy transfer rate that are in the SI. We note that in these simulations, we did not consider (i) the in-plane anisotropy of BP because the orientation of dipole moments of QDs are random (ii) the effect of BP thickness because the PL lifetime of QDs were nearly invariant for a wide range of BP thickness that included the thickness used in this study (see the SI).

In summary, we demonstrate long-range Förster-type energy transfer from a self-assembled monolayer of CdS/ZnS QDs to 3D BP through an AlO_x encapsulation layer, with a shallow distance dependence of $\sim d^{-2.3}$ and a Forster radius of 11.0 nm. We attribute the robust EnT over relatively long distances to electrodynamic interactions among QDs within the monolayer, which effectively increase the interfacial area over the donor and acceptor. Correspondence between experimental and simulated results suggest that specific parameters of the solid-state donor-acceptor system – the dimensionality of both the donor and acceptor – can be tuned in order to lengthen the distance over which high-yield EnT occurs. Therefore, this work provides design principles for the photosensitization of ambient-reactive materials through the encapsulation layer. More broadly, it provides a general theoretical framework for evaluating Förster parameters for various mixed dimensional systems consisting of bulk, thin-film, and self-assembled nanomaterials.

Acknowledgements. The experimental portion of this research was supported by the Northwestern University Materials Research Science and Engineering Center (MRSEC) (NSF DMR-1720139). The theory development and simulation portion of this research was supported by NSF grant CHE-205565. This work made use of the EPIC facility of Northwestern University's NUANCE Center, which has received support from the SHyNE Resource (NSF ECCS-2025633), the IIN, and Northwestern's MRSEC program (NSF DMR-1720139).

Supporting Information. The Supporting Information is available free of charge at https://pubs.acs.org.

Details of sample synthesis and preparation, atomic layer deposition, morphology of QD film, fluorescence lifetime measurements and analysis, theoretical derivations of EnT rate, FDTD simulation details.

REFERENCES.

- (1) Gusmão, R.; Sofer, Z.; Pumera, M. Black Phosphorus Rediscovered: From Bulk Material to Monolayers. *Angew. Chem. Int. Ed.* **2017**, *56* (28), 8052–8072. https://doi.org/10.1002/anie.201610512.
- (2) Xia, F.; Wang, H.; Jia, Y. Rediscovering Black Phosphorus as an Anisotropic Layered Material for Optoelectronics and Electronics. *Nat. Commun.* **2014**, *5* (1), 4458. https://doi.org/10.1038/ncomms5458.

- (3) Favron, A.; Gaufrès, E.; Fossard, F.; Phaneuf-L'Heureux, A.-L.; Tang, N. Y.-W.; Lévesque, P. L.; Loiseau, A.; Leonelli, R.; Francoeur, S.; Martel, R. Photooxidation and Quantum Confinement Effects in Exfoliated Black Phosphorus. *Nat. Mater.* **2015**, *14* (8), 826–832. https://doi.org/10.1038/nmat4299.
- (4) Wood, J. D.; Wells, S. A.; Jariwala, D.; Chen, K.-S.; Cho, E.; Sangwan, V. K.; Liu, X.; Lauhon, L. J.; Marks, T. J.; Hersam, M. C. Effective Passivation of Exfoliated Black Phosphorus Transistors against Ambient Degradation. *Nano Lett.* **2014**, *14* (12), 6964–6970. https://doi.org/10.1021/nl5032293.
- (5) Abate, Y.; Akinwande, D.; Gamage, S.; Wang, H.; Snure, M.; Poudel, N.; Cronin, S. B. Recent Progress on Stability and Passivation of Black Phosphorus. *Adv. Mater.* **2018**, *30* (29), 1704749. https://doi.org/10.1002/adma.201704749.
- (6) Castellanos-Gomez, A. Black Phosphorus: Narrow Gap, Wide Applications. *J. Phys. Chem. Lett.* **2015**, *6* (21), 4280–4291. https://doi.org/10.1021/acs.jpclett.5b01686.
- (7) Zhang, S.; Li, Y.; Zhang, X.; Dong, N.; Wang, K.; Hanlon, D.; N. Coleman, J.; Zhang, L.; Wang, J. Slow and Fast Absorption Saturation of Black Phosphorus: Experiment and Modelling. *Nanoscale* **2016**, *8* (39), 17374–17382. https://doi.org/10.1039/C6NR06076E.
- (8) Engel, M.; Steiner, M.; Avouris, P. Black Phosphorus Photodetector for Multispectral, High-Resolution Imaging. *Nano Lett.* **2014**, *14* (11), 6414–6417. https://doi.org/10.1021/nl502928y.
- (9) Guo, Q.; Pospischil, A.; Bhuiyan, M.; Jiang, H.; Tian, H.; Farmer, D.; Deng, B.; Li, C.; Han, S.-J.; Wang, H.; Xia, Q.; Ma, T.-P.; Mueller, T.; Xia, F. Black Phosphorus Mid-Infrared Photodetectors with High Gain. *Nano Lett.* **2016**, *16* (7), 4648–4655. https://doi.org/10.1021/acs.nanolett.6b01977.
- (10) Padgaonkar, S.; Olding, J. N.; Lauhon, L. J.; Hersam, M. C.; Weiss, E. A. Emergent Optoelectronic Properties of Mixed-Dimensional Heterojunctions. *Acc. Chem. Res.* **2020**. https://doi.org/10.1021/acs.accounts.9b00581.
- (11) Sangwan, V. K.; Hersam, M. C. Electronic Transport in Two-Dimensional Materials. *Annu. Rev. Phys. Chem.* **2018**, *69* (1), 299–325. https://doi.org/10.1146/annurev-physchem-050317-021353.
- (12) Sauer, K. Photosynthetic Membranes. *Acc. Chem. Res.* **1978**, *11* (7), 257–264. https://doi.org/10.1021/ar50127a001.
- (13) Taghipour, N.; Hernandez Martinez, P. L.; Ozden, A.; Olutas, M.; Dede, D.; Gungor, K.; Erdem, O.; Kosku Perkgoz, N.; Demir, H. V. Near-Unity Efficiency Energy Transfer from Colloidal Semiconductor Quantum Wells of CdSe/CdS Nanoplatelets to A Monolayer of MoS2. *ACS Nano* **2018**. https://doi.org/10.1021/acsnano.8b04119.
- (14) Konstantatos, G.; Badioli, M.; Gaudreau, L.; Osmond, J.; Bernechea, M.; de Arquer, F. P. G.; Gatti, F.; Koppens, F. H. L. Hybrid Graphene–Quantum Dot Phototransistors with Ultrahigh Gain. *Nat. Nanotechnol.* **2012**, *7* (6), 363–368. https://doi.org/10.1038/nnano.2012.60.
- (15) Jariwala, D.; Marks, T. J.; Hersam, M. C. Mixed-Dimensional van Der Waals Heterostructures. *Nat. Mater.* **2017**, *16* (2), 170–181. https://doi.org/10.1038/nmat4703.
- (16) Gaudreau, L.; Tielrooij, K. J.; Prawiroatmodjo, G. E. D. K.; Osmond, J.; de Abajo, F. J. G.; Koppens, F. H. L. Universal Distance-Scaling of Nonradiative Energy Transfer to Graphene. *Nano Lett.* **2013**, *13* (5), 2030–2035. https://doi.org/10.1021/nl400176b.

- (17) Chen, Z.; Berciaud, S.; Nuckolls, C.; Heinz, T. F.; Brus, L. E. Energy Transfer from Individual Semiconductor Nanocrystals to Graphene. *ACS Nano* **2010**, *4* (5), 2964–2968. https://doi.org/10.1021/nn1005107.
- (18) Prins, F.; Goodman, A. J.; Tisdale, W. A. Reduced Dielectric Screening and Enhanced Energy Transfer in Single- and Few-Layer MoS2. *Nano Lett.* **2014**, *14* (11), 6087–6091. https://doi.org/10.1021/nl5019386.
- (19) Raja, A.; Montoya-Castillo, A.; Zultak, J.; Zhang, X. X.; Ye, Z.; Roquelet, C.; Chenet, D. A.; Van Der Zande, A. M.; Huang, P.; Jockusch, S.; Hone, J.; Reichman, D. R.; Brus, L. E.; Heinz, T. F. Energy Transfer from Quantum Dots to Graphene and MoS2: The Role of Absorption and Screening in Two-Dimensional Materials. *Nano Lett.* **2016**, *16* (4), 2328–2333. https://doi.org/10.1021/acs.nanolett.5b05012.
- (20) Li, M.; Chen, J.-S.; Cotlet, M. Light-Induced Interfacial Phenomena in Atomically Thin 2D van Der Waals Material Hybrids and Heterojunctions. *ACS Energy Lett.* **2019**, *4* (9), 2323–2335. https://doi.org/10.1021/acsenergylett.9b01399.
- (21) Zang, H.; Routh, P. K.; Huang, Y.; Chen, J. S.; Sutter, E.; Sutter, P.; Cotlet, M. Nonradiative Energy Transfer from Individual CdSe/ZnS Quantum Dots to Single-Layer and Few-Layer Tin Disulfide. *ACS Nano* **2016**, *10* (4), 4790–4796. https://doi.org/10.1021/acsnano.6b01538.
- (22) Federspiel, F.; Froehlicher, G.; Nasilowski, M.; Pedetti, S.; Mahmood, A.; Doudin, B.; Park, S.; Lee, J. O.; Halley, D.; Dubertret, B.; Gilliot, P.; Berciaud, S. Distance Dependence of the Energy Transfer Rate from a Single Semiconductor Nanostructure to Graphene. *Nano Lett.* **2015**, *15* (2), 1252–1258. https://doi.org/10.1021/nl5044192.
- (23) Zhou, H.; Qin, C.; Chen, R.; Zhou, W.; Zhang, G.; Gao, Y.; Xiao, L.; Jia, S. Accurate Investigation on the Fluorescence Resonance Energy Transfer between Single Organic Molecules and Monolayer WSe2 by Quantum Coherent Modulation-Enhanced Single-Molecule Imaging Microscopy. *J. Phys. Chem. Lett.* 2019, 10 (11), 2849–2856. https://doi.org/10.1021/acs.jpclett.9b00854.
- (24) Liu, H.; Wang, T.; Wang, C.; Liu, D.; Luo, J. Exciton Radiative Recombination Dynamics and Nonradiative Energy Transfer in Two-Dimensional Transition-Metal Dichalcogenides. *J. Phys. Chem. C* **2019**, *123* (15), 10087–10093. https://doi.org/10.1021/acs.jpcc.8b12179.
- (25) Prasai, D.; Klots, A. R.; Newaz, A.; Niezgoda, J. S.; Orfield, N. J.; Escobar, C. A.; Wynn, A.; Efimov, A.; Jennings, G. K.; Rosenthal, S. J.; Bolotin, K. I. Electrical Control of Near-Field Energy Transfer between Quantum Dots and Two-Dimensional Semiconductors. *Nano Lett.* **2015**, *15* (7), 4374–4380. https://doi.org/10.1021/acs.nanolett.5b00514.
- (26) Li, M.; Chen, J.-S.; Routh, P. K.; Zahl, P.; Nam, C.-Y.; Cotlet, M. Distinct Optoelectronic Signatures for Charge Transfer and Energy Transfer in Quantum Dot–MoS2 Hybrid Photodetectors Revealed by Photocurrent Imaging Microscopy. *Adv. Funct. Mater.* **2018**, 28 (29), 1707558. https://doi.org/10.1002/adfm.201707558.
- (27) Ra, H.-S.; Kwak, D.-H.; Lee, J.-S. A Hybrid MoS2 Nanosheet–CdSe Nanocrystal Phototransistor with a Fast Photoresponse. *Nanoscale* **2016**, *8* (39), 17223–17230. https://doi.org/10.1039/C6NR05393A.
- (28) Gough, J. J.; McEvoy, N.; O'Brien, M.; Bell, A. P.; McCloskey, D.; Boland, J. B.; Coleman, J. N.; Duesberg, G. S.; Bradley, A. L. Dependence of Photocurrent Enhancements in Quantum Dot (QD)-Sensitized MoS2Devices on MoS2Film Properties. *Adv. Funct. Mater.* **2018**, *28* (13), 1706149. https://doi.org/10.1002/adfm.201706149.

- (29) Lee, T.; Enomoto, K.; Ohshiro, K.; Inoue, D.; Kikitsu, T.; Hyeon-Deuk, K.; Pu, Y.-J.; Kim, D. Controlling the Dimension of the Quantum Resonance in CdTe Quantum Dot Superlattices Fabricated via Layer-by-Layer Assembly. *Nat. Commun.* **2020**, *11* (1), 5471. https://doi.org/10.1038/s41467-020-19337-0.
- (30) Goodfellow, K. M.; Chakraborty, C.; Sowers, K.; Waduge, P.; Wanunu, M.; Krauss, T.; Driscoll, K.; Vamivakas, A. N. Distance-Dependent Energy Transfer between CdSe/CdS Quantum Dots and a Two-Dimensional Semiconductor. *Appl. Phys. Lett.* **2016**, *108* (2), 021101. https://doi.org/10.1063/1.4939845.
- (31) Flamee, S.; Cirillo, M.; Abe, S.; De Nolf, K.; Gomes, R.; Aubert, T.; Hens, Z. Fast, High Yield, and High Solid Loading Synthesis of Metal Selenide Nanocrystals. *Chem. Mater.* **2013**, *25* (12), 2476–2483. https://doi.org/10.1021/cm400799e.
- (32) Talapin, D. V.; Mekis, I.; Götzinger, S.; Kornowski, A.; Benson, O.; Weller, H. CdSe/CdS/ZnS and CdSe/ZnSe/ZnS Core—Shell—Shell Nanocrystals. *J. Phys. Chem. B* **2004**, *108* (49), 18826–18831. https://doi.org/10.1021/jp046481g.
- (33) Wells, S. A.; Henning, A.; Gish, J. T.; Sangwan, V. K.; Lauhon, L. J.; Hersam, M. C. Suppressing Ambient Degradation of Exfoliated InSe Nanosheet Devices via Seeded Atomic Layer Deposition Encapsulation. *Nano Lett.* **2018**, *18* (12), 7876–7882. https://doi.org/10.1021/acs.nanolett.8b03689.
- (34) Abellán, G.; Wild, S.; Lloret, V.; Scheuschner, N.; Gillen, R.; Mundloch, U.; Maultzsch, J.; Varela, M.; Hauke, F.; Hirsch, A. Fundamental Insights into the Degradation and Stabilization of Thin Layer Black Phosphorus. *J. Am. Chem. Soc.* **2017**, *139* (30), 10432–10440. https://doi.org/10.1021/jacs.7b04971.
- (35) McPhail, M. R.; Campbell, G. P.; Bedzyk, M. J.; Weiss, E. A. Structural Features of PbS Nanocube Monolayers upon Treatment with Mono- and Dicarboxylic Acids and Thiols at a Liquid–Air Interface. *Langmuir* **2016**, *32* (26), 6666–6673. https://doi.org/10.1021/acs.langmuir.6b01444.
- (36) Lee, A.-Y.; Ra, H.-S.; Kwak, D.-H.; Jeong, M.-H.; Park, J.-H.; Kang, Y.-S.; Chae, W.-S.; Lee, J.-S. Hybrid Black Phosphorus/Zero-Dimensional Quantum Dot Phototransistors: Tunable Photodoping and Enhanced Photoresponsivity. *ACS Appl. Mater. Interfaces* **2018**, *10* (18), 16033–16040. https://doi.org/10.1021/acsami.8b03285.
- (37) Energy Transfer. In *Principles of Fluorescence Spectroscopy*; Lakowicz, J. R., Ed.; Springer US: Boston, MA, 2006; pp 443–475. https://doi.org/10.1007/978-0-387-46312-4 13.
- (38) Swathi, R. S.; Sebastian, K. L. Distance Dependence of Fluorescence Resonance Energy Transfer. *J. Chem. Sci.* **2009**, *121* (5), 777. https://doi.org/10.1007/s12039-009-0092-x.
- (39) Kuhn, H. Classical Aspects of Energy Transfer in Molecular Systems. *J. Chem. Phys.* **1970**, *53* (1), 101–108. https://doi.org/10.1063/1.1673749.
- (40) Hua, X. M.; Gersten, J. I.; Nitzan, A. Theory of Energy Transfer between Molecules near Solid State Particles. *J. Chem. Phys.* **1985**, *83* (7), 3650–3659. https://doi.org/10.1063/1.449120.
- (41) Govorov, A. O.; Lee, J.; Kotov, N. A. Theory of Plasmon-Enhanced F\"orster Energy Transfer in Optically Excited Semiconductor and Metal Nanoparticles. *Phys. Rev. B* **2007**, 76 (12), 125308. https://doi.org/10.1103/PhysRevB.76.125308.
- (42) Yadav, R. K.; Bourgeois, M. R.; Cherqui, C.; Juarez, X. G.; Wang, W.; Odom, T. W.; Schatz, G. C.; Basu, J. K. Room Temperature Weak-to-Strong Coupling and the

- Emergence of Collective Emission from Quantum Dots Coupled to Plasmonic Arrays. *ACS Nano* **2020**, *14* (6), 7347–7357. https://doi.org/10.1021/acsnano.0c02785.
- (43) Zhang, X.; Marocico, C. A.; Lunz, M.; Gerard, V. A.; Gun'ko, Y. K.; Lesnyak, V.; Gaponik, N.; Susha, A. S.; Rogach, A. L.; Bradley, A. L. Experimental and Theoretical Investigation of the Distance Dependence of Localized Surface Plasmon Coupled Förster Resonance Energy Transfer. *ACS Nano* **2014**, *8* (2), 1273–1283. https://doi.org/10.1021/nn406530m.